Nanoscale

Iron nanoparticle templates for constructing 3D graphene framework with enhanced performance in sodium-ion batteries

Journal:	*Nanoscale*
Manuscript ID	NR-ART-08-2020-005682.R1
Article Type:	Paper
Date Submitted by the Author:	25-Sep-2020
Complete List of Authors:	Campeon, Benoit; Okayama University, Research Core for Interdisciplinary Sciences Chen, Wang; Okayama University, Research Core for Interdisciplinary Sciences Nishina, Yuta; Okayama University, Research Core for Interdisciplinary Sciences

ARTICLE

Iron nanoparticle templates for constructing 3D graphene framework with enhanced performance in sodium-ion batteries

Received 00th January 20xx,
Accepted 00th January 20xx

DOI: 10.1039/x0xx00000x

Benoît D.L. Campéon,[a‡] Chen Wang,[b‡] Yuta Nishina[ab*]

This study examines the synthesis and electrochemical performance of three-dimensional graphene for Li-ion batteries and Na-ion batteries. The in-situ formation of iron hydroxide nanoparticles ($Fe(OH)_x$ NPs) of various weights on the surface of graphene oxide, followed by thermal treatment at elevated temperature and washing using hydrochloric acid, furnished 3D graphene. The characterization confirmed the prevention of graphene layers stacking by over 90% compared with thermal treatment without $Fe(OH)_x$. The electrochemical performance of the 3D graphene was evaluated as a counter electrode for lithium metal and sodium metal in a half-cell configuration. This material showed good performances with a charging capacity of 507 mAh g^{-1} at 372 mA g^{-1} in Li-ion battery and 252 mAh g^{-1} at 100 mA g^{-1} in Na-ion battery, which is 1.4 and 1.9 times higher, respectively, than the graphene prepared without $Fe(OH)_x$ templates.

1. Introduction

Graphene, a single atomic layer of sp^2-bonded carbons in a honeycomb crystal lattice, is the thinnest material found in the world so far. Geim and Novoselov obtained it first by repeatedly cleaving graphite with adhesive tape in their ground-breaking research on two-dimensional materials.[1–3] Due to its particular properties, such as the high theoretical surface area of 2630 m^2 g^{-1} and high electron mobility of 2,000,000 cm^2 $V^{-1}S^{-1}$, graphene has been intensively researched to design next-generation devices.[4–8]

The research on its applications, such as high-speed transistors,[9] high-sensitivity sensors,[10] touch-panels,[11] high-efficiency solar cells, and rechargeable batteries,[12–16] are growing explosively all over the world. To meet the demand for various applications, large-scale production of graphene needs to be developed. A chemical vapor deposition (CVD) method can furnish high-quality graphene; however, its cost and its production scale limit its practical application.[17,18] The direct exfoliation of graphite can provide low-defect graphene but with a broad thickness distribution.[19] The most effective method to obtain graphene at a relatively low cost and on a large scale is the successive oxidation and exfoliation of graphite to produce graphene oxide (GO), and its reduction.[8,20] Functional groups attached on its surface, such as hydroxy, carboxy, and epoxy groups, can be modified to tune its properties.[21–23] Lowering the amount of oxygen on GO provides graphene-like materials. Two types of reduction methods, so-called liquid phase and solid phase reductions, have been developed. In the former method, GO can be well dispersed in solvent in the presence of reducing agent or solvothermal treatment is performed. The graphene sheets aggregate during the reduction, forming block- or flower-like structures.[24,25] The solid phase reduction is achieved by thermal treatment or photo-irradiation to the dried GO under vacuum or inert gas environment. The dried GO sheets overlap with each other. As the reduction proceeds, the oxygen functional groups that keep the exfoliated state are removed, causing the graphene sheets' re-stacking. [26,27]

Among all rechargeable batteries, Li-ion batteries (LIBs) certainly improved our lives with their high energy density, tiny memory effect, and low self-discharge. Since the commercialization of LIBs in 1990, graphite electrode has been used as an anode material despite its small theoretical capacity of 372 mAh g^{-1}.[28] The small interlayer distance of graphite induces a limited storage space, as well as a narrow diffusion pathway for the Li ions, leading to its small electric capacity and low rate capability. Furthermore, the small distance between graphite layers hampers the utilization of Na ions, which are more abundant in resources than Li ions.[29–33] Therefore, the aim of research in the area of rechargeable batteries is the development of high capacity electrodes with adequate space between graphene layers.

To address these issues, graphene emerged as a candidate material to provide higher energy and power density LIBs and Na-ion batteries (SIBs). Indeed, it is considered that graphene can adsorb ions on both sides and defect sites.[28,34] However, the aggregation and re-stacking lead to a much smaller specific surface area than the theoretical value. As a result, the space and pathway for ion storage and mobility are reduced, leading to a small capacity and low rate capability. In the present work, we report a cost-effective and scalable approach to produce 3D graphene architectures, which are unstacked forms of reduced

[a] Graduate School of Natural Science and Technology, Okayama University, 3-1-1 Tsushima-Naka, Kita-Ku, Okayama, 700-8530, Japan.
[b] Research Core for Interdisciplinary Sciences, Okayama University, 3-1-1 Tsushima-Naka, Kita-Ku, Okayama, 700-8530, Japan.
‡ These authors contributed equally.
† Electronic Supplementary Information (ESI) available: [details of any supplementary information available should be included here]. See DOI: 10.1039/x0xx00000x

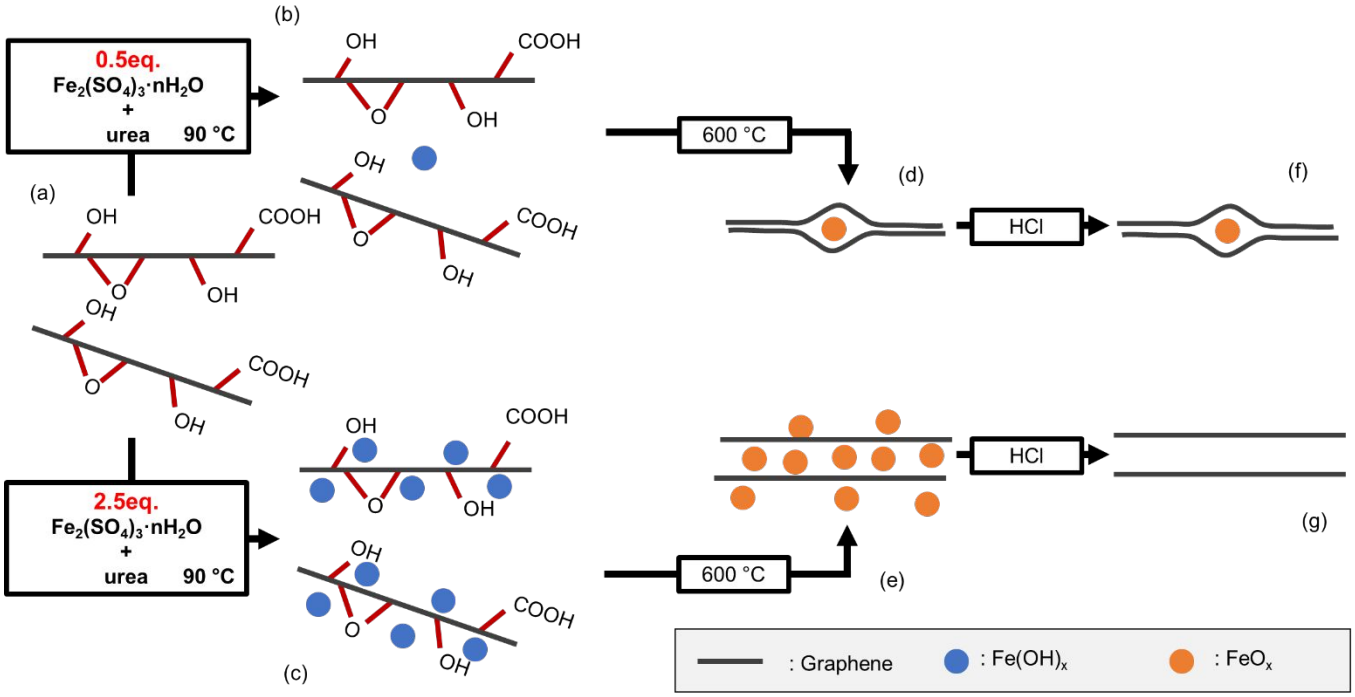

Fig. 1. rGO synthesis: (a) GO, (b) GO-$Fe(OH)_{0.5}$, (c) GO-$Fe(OH)_{2.5}$, (d) rGO-$FeO_{0.5}$, (e) rGO-$FeO_{2.5}$, (f) $G_{0.5}$, (g) $G_{2.5}$.

graphene oxide (rGO) with the aid of iron oxide nanoparticles (FeO_x NPs) between graphene layers. Initially, GO, urea, and $Fe_2(SO_4)_3 \cdot nH_2O$ were mixed and heated in water to form GO-$Fe(OH)_x$. Then it was dried and thermally treated under N_2 to form rGO-FeO_x. Finally, iron was etched with aq. HCl to form 3D graphene. This research demonstrates that adjusting the ratio of $Fe_2(SO_4)_3 \cdot nH_2O$ and GO (Fe/GO), and the heating temperature enables the formation of excellent materials for LIBs, displaying 745 mAh g^{-1} at 372 mA g^{-1} instead of 525 mAh g^{-1}, as well as for SIBs, expressing 362 mAh g^{-1} at 100 mA g^{-1} instead of 173 mAh g^{-1}. This synthesis approach presents a promising route for the large-scale production of rGO as electrode materials for SIBs.

2. Results and discussion

The 3D graphene was prepared in four steps, as illustrated in Fig. 1. For the first step, highly dispersible GO was prepared from graphite by our modified Hummers' method (Fig. 1a and Fig. S1 †).[20,35] In the second step, iron hydroxide nanoparticles ($Fe(OH)_x$ NPs) were formed on the surface of the GO layer by heating the GO, $Fe_2(SO_4)_3 \cdot nH_2O$, and urea in water at 90 °C for 2 hours (Fig. 1b,c).[36] The formed GO-$Fe(OH)_x$ composite was collected by centrifugation, and then freeze-dried. The obtained materials were termed GO-$Fe(OH)_x$ (x= 0.5, 1.0, 1.5, 2.5). In the third step, GO-$Fe(OH)_x$ was thermally treated under N_2 atmosphere to form unstacked rGO and FeO_x composite (rGO-FeO_x), where the GO reduction and FeO_x NPs formation occurred simultaneously (Fig. 1 d,e). The FeO_x NPs worked as spacers to prevent the re-stacking of graphene sheets. The samples were prepared by introducing various $Fe_2(SO_4)_3 \cdot nH_2O$ amounts: 0 eq., 0.5 eq., 1 eq., 1.5 eq., and 2.5 eq. of the weight of GO, respectively. These were termed rGO and rGO-FeO_x (x= 0.5, 1.0, 1.5, 2.5). The temperature of thermal treatment was investigated from 90 to 600 °C. In the last step, 3D graphene was obtained by washing FeO_x NPs out with concentrated hydrochloric acid (Fig. 1f, g). Obtained samples were termed G_x (x= 0.5, 1.0, 1.5, 2.5).

2.1. Iron NPs synthesis.

As the role of iron NPs is the cornerstone of this strategy, its synthesis was initially optimized. The formation of $Fe(OH)_x$ NPs was investigated using NH_3 or urea.[36] In both approaches, $Fe(OH)_x$ was obtained by the reaction of iron ions with hydroxyl ions. In the former situation, dense $Fe(OH)_x$ particles were obtained (Fig. 2a, b). In contrast, urea produced a fluffy $Fe(OH)_x$ composed of needle-like particles that were expected to widen the distance between graphene interlayers (Fig. 2d, e). In the case of urea treatment, we noticed that the walls of the reactors were uniformly coated with the orange colour of $Fe(OH)_x$, suggesting the slow formation of $Fe(OH)_x$ translating the uniform formation of GO-Fe(OH). In contrast, in the case of NH_3, nothing was formed on the walls. Therefore, we concluded that the $Fe(OH)_x$ was slowly formed, and uniform production of GO-$Fe(OH)_x$ was achieved when urea was used. X-ray diffraction (XRD) for the iron hydroxide compounds prepared by urea or NH_3 showed completely different patterns: NH_3 provided amorphous $Fe(OH)_x$, while urea provided crystalline $Fe(OH)_x$ (Fig. S2iii, iv †), supporting the slow and uniform formation of $Fe(OH)_x$ by urea.

After 600 °C thermal treatment under N_2, $Fe(OH)_x$ prepared with both NH_3 and urea turned into similar FeO_x particles (Fig.

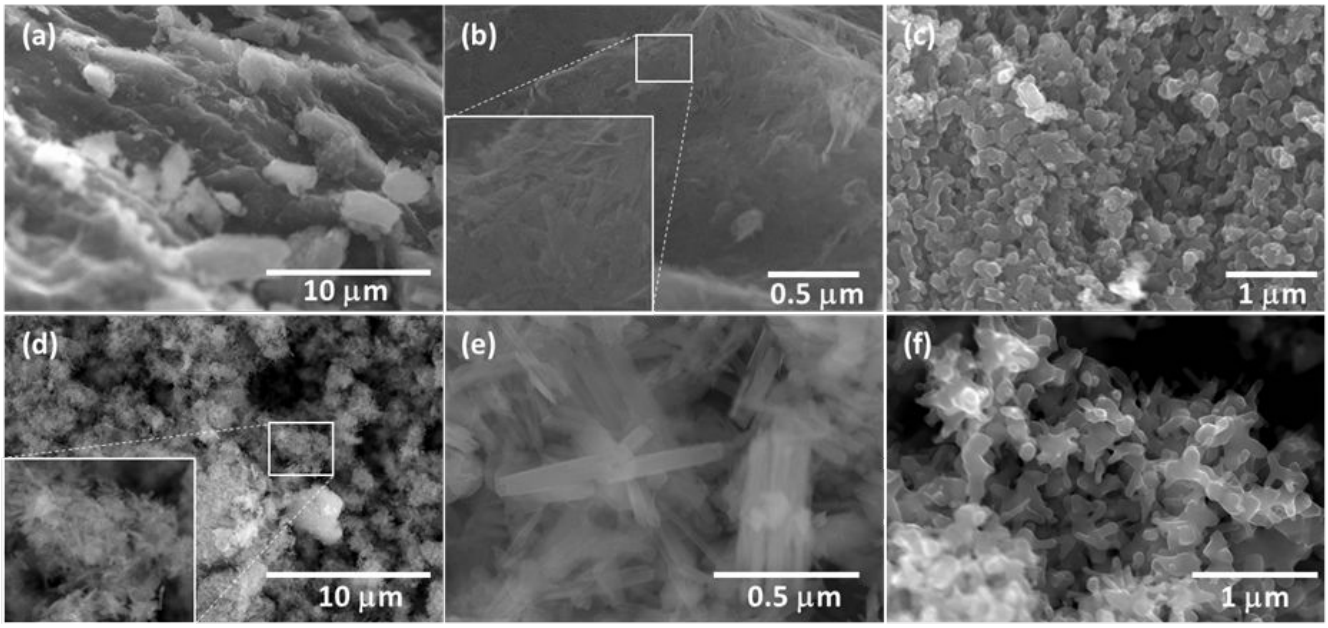

Fig. 2. SEM images: (a) aggregated $Fe(OH)_x$ produced by NH_3, (b) corresponding magnified image, (c) FeO_x obtained by NH_3 method, (d) needle-like $Fe(OH)_x$ produced by urea, (e) corresponding magnified image, (f) FeO_x obtained by urea method.

2c, f). XRD analysis revealed Fe_3O_4 was mainly formed (Fig. S2i, ii †).[37] A stronger intensity and sharper peak were observed on the sample prepared by the urea method, indicating its higher crystallinity.

Based on the above investigations, we decided to use the urea method to synthesize GO-$Fe(O)H_x$ composites for the subsequent studies.

2.2. Synthesis and characterization of rGO-FeO_X.

We investigated the structural change by thermal treatment from 90 to 600 °C for GO-$Fe(OH)_{1.0}$. The chemical state and elemental composition were observed by X-ray photoelectron spectroscopy (XPS) (Fig. 3a). The C 1s region of GO-$Fe(OH)_{10}$ could be separated into three waveforms, 284.5 eV, 286.6 eV, and 288.3 eV, which were considered C-C, C-O, and C=O, respectively.[8,20,38] As the temperature increased, the intensity of C-O and C=O decreased.[39] The oxygen, carbon, and iron atomic ratios were obtained by peak area quantification of XPS data (Fig. 3b). Heating at higher than 500 °C produced an oxygen concentration below 10%. Far lower Fe contents than expected were obtained in the XPS measurement for all the samples (Fig. 3b) due to the features of XPS measurement (i.e., XPS can only provide surface information). This result suggests that iron particles are present inside the GO layers. To confirm this hypothesis, we used an argon ion beam to etch the surface systematically, and measured XPS accordingly (Fig. S3 †). All the samples showed two peaks attributed to Fe 2p3/2 and Fe 2p1/2, respectively, which were split by spin-orbit interaction. The iron peaks were very weak in the spectrum for the measurement of the composite surface prior to etching because surface iron species were washed off during the purification treatment. After etching, the peaks of Fe 2p3/2 and Fe 2p1/2 suddenly became stronger, indicating that iron was located inside the layers of rGO. Furthermore, even after several etchings, the intensity of peaks became constant, demonstrating that the amount of iron particles contained inside the rGO interlayer was uniform.

The structural change of rGO and the formation of FeO_x were investigated at different temperatures by XRD (Fig. 3c). It has been reported that GO shows a clear (002) diffraction peak at around $2\theta = 12°$, and it shifts at around 26° by reduction.[8,40,41] As shown in Fig. 3c, all the (002) peaks of rGO-$FeO_{1.0}$ were weak and broad, suggesting the iron particles were well anchored between GO sheets. Treatment of GO-$Fe(OH)_{1.0}$ at 90 °C (Fig. 3ci) showed a small GO-like (002) diffraction at $2\theta = 12°$, meaning that the reduction of GO was not completed. Increasing the temperature to 120 °C was enough to reduce the GO (002) peak (Fig. 3cii). By a further temperature increase, the peak of graphite appeared and became sharper and closer to 26°, suggesting the partial graphitization in rGO-$FeO_{1.0}$ (Fig. 3ciii-viii). In the following section, rGO-FeO_x were prepared at 600 °C.

To prevent the graphitization, the amount of iron was investigated. The degree of rGO stacking was investigated by XRD for rGO-FeO_x with various iron contents treated at 600 °C (Fig. 3d). By introducing only 0.5 eq. iron to the weight of GO, the (002) peak of rGO-$FeO_{0.5}$ became smaller, about 18% of rGO without iron (Fig. 3e). As the amount of iron was increased, the (002) peak weakened and almost disappeared with 2.5 eq. iron to the weight of GO, reaching only 3% of rGO without iron. These results support the hypothesis that the in-situ formation of $Fe(OH)_x$ NPs between GO sheets lowers the stacking of rGO sheets during thermal reduction.

The morphology of rGO-FeO_x was observed by scanning electron microscopy (SEM) and transmission electron microscopy (TEM) (Fig. S4 † and Fig. 3f). SEM and TEM both confirmed the formation of FeO_x NPs. More interestingly, larger numbers of particles were observed for TEM than SEM,

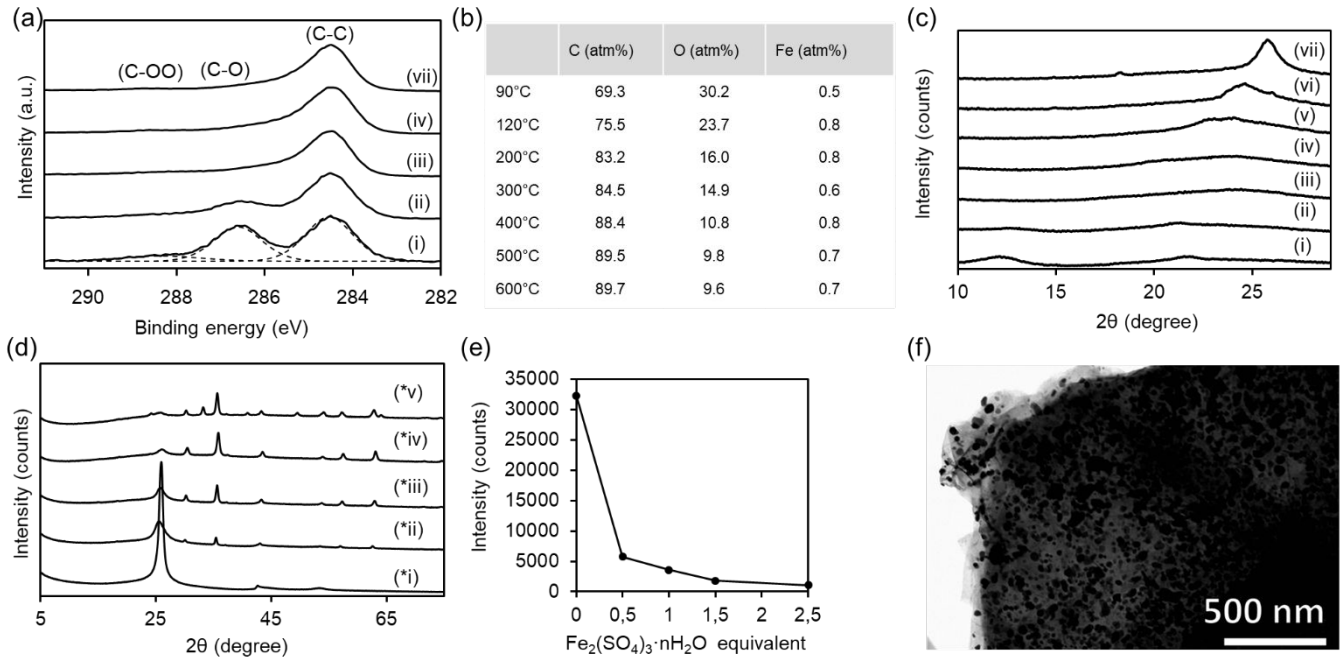

	C (atm%)	O (atm%)	Fe (atm%)
90°C	69.3	30.2	0.5
120°C	75.5	23.7	0.8
200°C	83.2	16.0	0.8
300°C	84.5	14.9	0.6
400°C	88.4	10.8	0.8
500°C	89.5	9.8	0.7
600°C	89.7	9.6	0.7

Fig. 3. (a) C 1s XPS of rGO-$FeO_{1.0}$ composites prepared at various temperatures. (b) Atomic concentration ratio of rGO-$Fe_{1.0}$ surface prepared by XPS. (c) XRD patterns of rGO-$FeO_{1.0}$ composites prepared at various temperatures: (i) before heating, (ii) 120 °C, (iii) 200 °C, (iv) 300 °C, (v) 400 °C, (vi) 500 °C, (vii) 600 °C. (d) XRD patterns of rGO-FeO_X composites prepared in various FeSO4· 7H2O amounts: (*i) 0 eq., (*ii) 0.5 eq., (*iii) 1 eq.%, (*iv) 1.5 eq., (*v) 2.5 eq. (e) intensity of rGO-FeO_x restacking XRD peak with various $FeSO_4$· $7H_2O$ amounts, (f) TEM image of rGO-$FeO_{1.5}$.

suggesting that FeO_x NPs were present inside the rGO layers since SEM can only detect the NPs on the surface.

2.3. Removal of FeO_x NPs from rGO-FeO_X.

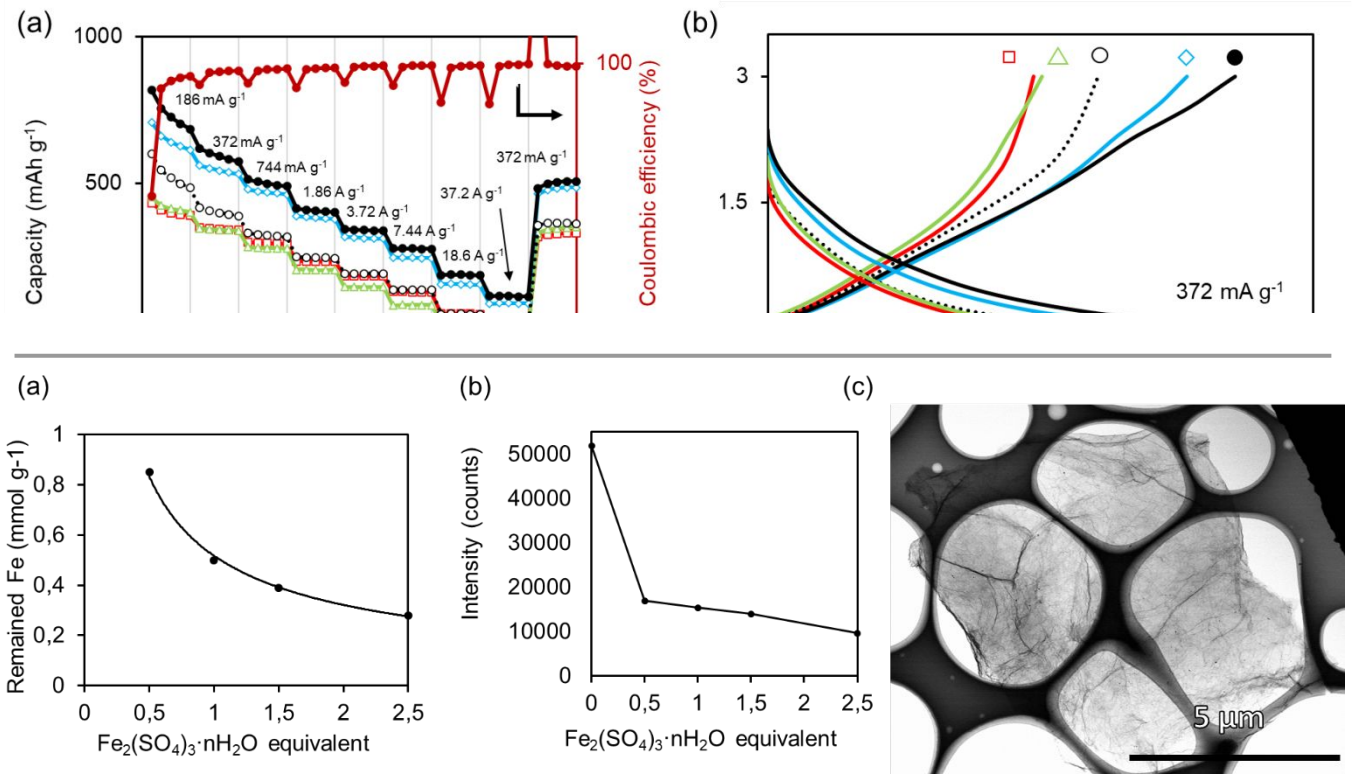

Fig. 4. (a) Atomic absorption of Fe from burned ashes of rGO-FeO_x with various iron amounts, (b) intensity of G_x restacking XRD peak with various $FeSO_4 \cdot 7H_2O$ amounts, (f) TEM image of $G_{1.5}$.

G_x was synthesized by washing out FeO_x from rGO-FeO_x using concentrated hydrochloric acid. After treatment, G_x could not be affected by a magnet. To confirm the remaining iron species content, G_x was analysed by atomic absorption spectroscopy (Fig. 4a). The result indicated that the amount of iron in $G_{2.5}$ was below 0.3 mmol g^{-1}. Interestingly, we observed that the amount of remaining iron decreased with the amount of iron originally present, indicating that it is more difficult to remove iron species from rGO-FeO_x prepared from a smaller iron amount. We believe that low iron loading on GO led to the formation of iron species wrapped by graphene, which were inaccessible to hydrochloric acid, while graphene could not wrap iron species when its amount was high, enabling the access to hydrochloric acid. The stacking degree of G_x was evaluated by XRD; the graphite (002) peak was reduced as the amount of iron increased (Fig. 4b and Fig. S5 †). With only 0.5 eq. $Fe_2(SO_4)_3 \cdot nH_2O$, the stacking was lowered by 68%, and with 2.5 eq. the stacking was lowered by 92%, demonstrating that G_x preserved the unstacked nature of rGO-FeO_x after the removal of FeO_x NPs. The specific surface area (SSA) measured by Brunauer-Emmett-Teller analysis of rGO and $G_{2.5}$ were conducted, the results show an increase of the SSA from 29 m^2 g^{-1} to 140 m^2 g^{-1} confirming that iron NPs can act as a spacer for GO reduction. The observation of G_x by SEM and TEM (Fig. 4c and Fig. S6 †) confirms the successful removal of FeO_x NPs when the amount of introduced $Fe_2(SO_4)_3 \cdot nH_2O$ was above 1.5eq., while lower amount results in trapped FeO_x NPs.

2.4. LIBs and SIBs evaluations.

The Li-ion and Na-ion storage capabilities of G_x were evaluated in a half-cell configuration using 2032-type coin cells. The electrodes were prepared using G_x as active materials and polyvinylidene fluoride as a binder without adding any conductive materials. A comparative study was conducted using rGO and G_x prepared with various iron contents by charge-discharge cycle tests at a current rate ranging from 0.186 to 37.2 A g^{-1} and from 20 to 400 mA g^{-1} for LIBs and SIBs, respectively.

For LIBs at 186 mA g^{-1}, rGO expressed a specific capacity of 600 mAh g^{-1}, while $G_{0.5}$ had a specific capacity of 453 mAh g^{-1} (Fig. 5a,b). The inferior performance of $G_{0.5}$ reflects the formation of non-accessible space for Li-ions. The specific capacity gradually increased with the increase of iron loading, reaching a maximum specific capacity of 750 mAh g^{-1} for $G_{2.5}$. At 3.72 A g^{-1}, the specific capacity of rGO decreased by 67%, reaching 200 mAh g^{-1} while the specific capacity of $G_{2.5}$ decreased by 53% to 350 mAh g^{-1}, denoting the superior capability of $G_{2.5}$ for high-rate LIB. After 45 cycles, at 372 mA g^{-1}, the capacity stabilized, and the charging capacity was 362 mAh g^{-1} for rGO and 507 mAh g^{-1} for $G_{2.5}$. The specific capacity increase was correlated with the increased charge-discharge potential between 0.8 V and 2.8 V (Fig. 5b). To determine whether FeO's trace amount contributes to the capacity, the potential has been plotted vs dC/dV for rGO, rGO-$FeO_{2.5}$, and $G_{2.5}$ (Fig. S7 †). Compared with rGO, rGO-$FeO_{2.5}$ shows a peak at 1.8 V due to FeO's presence whereas $G_{2.5}$ shows no peak confirming that FeO was efficiently removed from graphene and do not contribute to $G_{2.5}$ superior capacity.

For the SIBs evaluation at 20 mA g^{-1}, rGO, $G_{0.5}$, and $G_{1.0}$ expressed similar specific capacities of around 150 mAh g^{-1} (Fig.

5b,c). The low amount of FeO NPs did not improve the active surface of G_x for large ions (Na^+); therefore, there was no visible impact on the performance (Fig. 5c,d). In contrast, $G_{1.5}$ and $G_{2.5}$ showed increases of the specific capacity to 230 mAh g^{-1} and 297 mAh g^{-1}, respectively. At 400 mA g^{-1}, the specific capacity of rGO decreased by 55%, reaching 68 mAh g^{-1}, while the specific capacity of $G_{2.5}$ decreased by 52% to 143 mAh g^{-1} denoting the superior capability of $G_{2.5}$ for Na-ion batteries. After 30 cycles, the capacity stabilized, reaching a stable charge capacity performance at 100 mA g^{-1} of 130 mAh g^{-1} for rGO, while $G_{2.5}$ reached 252 mAh g^{-1}. The increase of charge specific capacity was correlated with the increased capacity between 0.3 V and 2.2 V (Fig. 5b), translating the improvement of Na^+ absorption in unstacked graphene layers. Compared with previously reported bare carbon host material for SIBs (Table S1 †), $G_{2.5}$ displays similar to superior capacity performances.[42–47]

These results demonstrate that the un-stacking of graphene layers and the formation of the graphene 3D structure improve the overall capacitor behavior, enabling more linear charge behavior. Unlocking the full capacitor behavior of graphene leads to superior capacity performance.

3. Conclusion

In summary, we have designed a simple, cost-effective, and scalable method for the synthesis of 3D graphene applying FeO_x NPs as inter-layer spacers. The synthesis of iron NPs was investigated using $Fe_2(SO_4)_3{\cdot}nH_2O$ as the iron source and urea or NH_3 as the base. The results revealed that directly using NH_3 formed aggregated and lower crystallinity NPs, while urea slowly decomposed into NH_3 led to the formation of iron NPs with a needle-like structure and superior crystallinity. Given these convincing results, the urea method was applied to GO aqueous dispersion, resulting in the formation of GO-$Fe(OH)_x$. The reduction of GO at high temperature in N_2 atmosphere led to the formation of rGO-FeO_x, while lowering the staking level of graphene layers by FeO_x NPs. Then, iron NPs were removed using HCl to obtain 3D graphene, which preserved the unstacked nature of the original rGO-FeO_x. In light of the positive result, the 3D graphene was applied to LIBs and SIBs, providing superior capacity and rate capability performances. The best results were obtained for $G_{2.5}$, which displayed 590 mAh g^{-1} at 372 mA g^{-1} for LIBs and 297 mAh g^{-1} at 20 mA g^{-1} for SIBs. Additionally, this successful strategy for the synthesis of 3D graphene should be of particular interest for membrane filtration application as it requires graphene materials with tailored size, interlayer spacing, and porosity.

4. Experimental section

4.1.Materials

Graphite (SP-10) was purchased from BAY CARBON Inc. $KMnO_4$, H_2SO_4, 30% aq. H_2O_2, hydrazine hydrate, HCl were purchased from Wako Pure Chemical Industries, Ltd. Iron(III) sulfate n-hydrate ($Fe_2(SO_4)_3{\cdot}nH_2O$) was purchased from KANTO CHEMICAL CO., INC. 1 M sodium hexafluorophosphate ($NaPF_6$), dissolved in 1/1 (V/V) ethylene carbonate (EC)/diethyl carbonate (DEC) and 1 M lithium hexafluorophosphate ($LiPF_6$), dissolved in 1/1 (V/V) ethylene carbonate (EC)/diethyl carbonate (DEC) were purchased from Kishida Chemical Co., Ltd. Sodium was purchased from Sigma Aldrich. Lithium was purchased from Honjo Metal Co., Ltd. All reagents were used directly without further purification.

4.2. Graphene oxide (GO) synthesis.

GO was synthesized using our modified Hummers' method.[20] Natural flake graphite (3.0 g) was stirred in 95% H_2SO_4 (75 mL). $KMnO_4$ (9.0 g) was gradually added to the solution keeping the temperature <10 °C. The mixture was then stirred at 35 °C for 2 h. The resulting mixture was diluted by water (75 mL) under vigorous stirring and cooling so that temperature does not exceed 50 °C. The suspension was further treated by 30% aq. H_2O_2 (7.5 mL). The resulting suspension was purified by centrifugation with water until neutralization, and freeze-dried.

4.3. 3D graphene (G) synthesis.

In the first step, iron hydroxide was formed on the surface of the GO layer. In a 0.5 wt% GO aqueous dispersion, $Fe_2(SO_4)_3{\cdot}nH_2O$ (0.5 to 2.5 weight equivalent of GO) and urea (1.1 weight equivalent of $Fe_2(SO_4)_3{\cdot}nH_2O$) were consecutively added and dispersed by sonication for 30 minutes. As prepared mixture was continuously stirred and heated at 90 °C for 2 hours. The composite was collected by filtration or centrifugation, then freeze-dried. In the second step, the thermal treatment (90 to 600 °C) was conducted under N_2 atmosphere. The temperature was increase form R.T to 200 °C in 1 hour, from 200 °C to target temperature with 19 °C min^{-1}, and kept at the target temperature for 30 minutes. In the last step, 3D graphene was obtained by washing out FeO_x particles with concentrated hydrochloric acid with the aid of sonication for 2 hours.

4.4. LIB preparation and evaluation.

The CR2032 coin cells were assembled in an Ar-filled glove box to evaluate the electrochemical performance of G_x samples as anode materials for lithium-ion batteries. The slurry was prepared by mixing G_x (90%) and of poly(vinylidene fluoride) binder (10%) in an N-methylpyrrolidone (NMP) as a solvent. The anode was produced by coating the slurry onto copper foil as flat film with a thickness of 0.1 mm by doctor blade. Thin Lithium foil (0.6 mm thick) was employed as the counter electrode and a glass microfiber was used as the separator. The electrolyte was 1 M lithium hexafluorophosphate ($LiPF_6$), dissolved in 1/1 (V/V) ethylene carbonate (EC)/diethyl carbonate (DEC). The coin cells were tested in galvanostatic mode at various currents within a voltage range of 0.01 V to 3.0 V using a 580 Battery Test System (Toyo corporation).

4.5. SIB preparation and evaluation.

The CR2032 coin cells were assembled in an Ar-filled glove box to evaluate the electrochemical performance of G_x samples as

anode materials for sodium-ion batteries. The slurry was prepared by mixing Gx (90%) and of poly(vinylidene fluoride) binder (10%) in an N-methylpyrrolidone (NMP) as a solvent. The anode was produced by coating the slurry onto copper foil as flat film with a thickness of 0.1 mm by doctor blade. Thin sodium foil (0.6 mm thick) was employed as the counter electrode and a glass microfiber was used as the separator. The electrolyte was 1 M sodium hexafluorophosphate ($NaPF_6$), dissolved in 1/1 (V/V) ethylene carbonate (EC)/diethyl carbonate (DEC). The coin cells were tested in galvanostatic mode at various currents within a voltage range of 0.01 V to 3.0 V using a 580 Battery Test System (Toyo corporation).

AUTHOR INFORMATION

Corresponding Author

* nisina-y@cc.okayama-u.ac.jp

Author Contributions

The manuscript was written through the contributions of all authors. All authors have given approval to the final version of the manuscript. ‡These authors contributed equally.

Funding Sources

JST CREST (JPMJCR18R3).

Notes

The authors declare no competing interest.

ACKNOWLEDGMENT

This research was supported by JST CREST (JPMJCR18R3).

REFERENCES

1 K. S. Novoselov, A. K. Geim, S. V. Morozov, D. Jiang, Y. Zhang, S. V. Dubonos, I. V. Grigorieva and A. A. Firsov, *Science*, 2004, **306**, 666–669.
2 K. S. Novoselov, *Rev. Mod. Phys.*, 2011, **83**, 837–849.
3 K. S. Novoselov and A. H. C. Neto, *Phys. Scr.*, 2012, **T146**, 014006.
4 M. D. Stoller, S. Park, Y. Zhu, J. An and R. S. Ruoff, *Nano Lett.*, 2008, **8**, 3498–3502.
5 K. E. Whitener and P. E. Sheehan, *Diamond and Related Materials*, 2014, **46**, 25–34.
6 K. I. Bolotin, K. J. Sikes, Z. Jiang, M. Klima, G. Fudenberg, J. Hone, P. Kim and H. L. Stormer, *Solid State Communications*, 2008, **146**, 351–355.
7 A. Sinitskii, A. Dimiev, D. A. Corley, A. A. Fursina, D. V. Kosynkin and J. M. Tour, *ACS Nano*, 2010, **4**, 1949–1954.
8 B. D. L. Campéon, M. Akada, M. S. Ahmad, Y. Nishikawa, K. Gotoh and Y. Nishina, *Carbon*, 2020, **158**, 356–363.
9 A. G. Kelly, T. Hallam, C. Backes, A. Harvey, A. S. Esmaeily, I. Godwin, J. Coelho, V. Nicolosi, J. Lauth, A. Kulkarni, S. Kinge, L. D. A. Siebbeles, G. S. Duesberg and J. N. Coleman, *Science*, 2017, **356**, 69–73.
10 Y. Wang, Y. Shao, D. W. Matson, J. Li and Y. Lin, *ACS Nano*, 2010, **4**, 1790–1798.
11 H. Tian, Y. Yang, D. Xie, T.-L. Ren, Y. Shu, C.-J. Zhou, H. Sun, X. Liu and C.-H. Zhang, *Nanoscale*, 2013, **5**, 890–894.
12 S. Sun, L. Gao and Y. Liu, *Appl. Phys. Lett.*, 2010, **96**, 083113.
13 G. Wang, X. Shen, J. Yao and J. Park, *Carbon*, 2009, **47**, 2049–2053.
14 H. Tan, X. Z. Yu, K. Huang, J. Zhong and B. Lu, *Journal of Energy Chemistry*, 2020, **51**, 388–395.
15 J. Ge, B. Wang, J. Zhou, S. Liang, A. M. Rao and B. Lu, *ACS Materials Lett.*, 2020, **2**, 853–860.
16 Z. Liu, J. Wang and B. Lu, *Science Bulletin*, 2020, **65**, 1242–1251.
17 S. J. Chae, F. Güneş, K. K. Kim, E. S. Kim, G. H. Han, S. M. Kim, H.-J. Shin, S.-M. Yoon, J.-Y. Choi, M. H. Park, C. W. Yang, D. Pribat and Y. H. Lee, *Advanced Materials*, 2009, **21**, 2328–2333.
18 T. Taira, T. Shinohara, S. Obata and K. Saiki, *Jpn. J. Appl. Phys.*, 2019, **58**, SIIB24.
19 P.-C. Lin, J.-Y. Wu and W.-R. Liu, *Scientific Reports*, 2018, **8**, 1–8.
20 N. Morimoto, T. Kubo and Y. Nishina, *Scientific Reports*, 2016, **6**, 21715.
21 M. Fang, K. Wang, H. Lu, Y. Yang and S. Nutt, *J. Mater. Chem.*, 2009, **19**, 7098–7105.
22 M. Z. I. Nizami, Y. Nishina, T. Yamamoto, Y. Shinoda-Ito and S. Takashiba, *J Dent Res*, 2020, **99**, 182–188.
23 R. Fujii, K. Okubo, S. Takashiba, A. Bianco and Y. Nishina, *Carbon*, 2020, **160**, 204–210.
24 Z. Wang, X. Zhou, J. Zhang, F. Boey and H. Zhang, *J. Phys. Chem. C*, 2009, **113**, 14071–14075.
25 M. S. Ahmad, H. He and Y. Nishina, *Org. Lett.*, 2019, **21**, 8164–8168.
26 H. C. Schniepp, J.-L. Li, M. J. McAllister, H. Sai, M. Herrera-Alonso, D. H. Adamson, R. K. Prud'homme, R. Car, D. A. Saville and I. A. Aksay, *J. Phys. Chem. B*, 2006, **110**, 8535–8539.
27 J. H. Lee, N. Park, B. G. Kim, D. S. Jung, K. Im, J. Hur and J. W. Choi, *ACS Nano*, 2013, **7**, 9366–9374.
28 K. Ji, J. Han, A. Hirata, T. Fujita, Y. Shen, S. Ning, P. Liu, H. Kashani, Y. Tian, Y. Ito, J. Fujita and Y. Oyama, *Nature Communications*, 2019, **10**, 1–10.
29 A. Yoshino, *Angew. Chem. Int. Ed*, 2012, **51**, 5798– 5800.
30 M. S. Whittingham, *Belgian patent no.*, 1975, 819672.
31 H. Li, L. Peng, Y. Zhu, D. Chen, X. Zhang and G. Yu, *Energy Environ. Sci.*, 2016, **9**, 3399–3405.
32 L. David, R. Bhandavat and G. Singh, *ACS Nano*, 2014, **8**, 1759–1770.
33 K. Mizushima, P. C. Jones, P. J. Wiseman and J. B. Goodenough, *Materials Research Bulletin*, 1980, **15**, 783–789.
34 K. Kubota, S. Shimadzu, N. Yabuuchi, S. Tominaka, S. Shiraishi, M. Abreu-Sepulveda, A. Manivannan, K. Gotoh, M. Fukunishi, M. Dahbi and S. Komaba, *Chem. Mater.*, , DOI:10.1021/acs.chemmater.9b05235.
35 N. Morimoto, H. Suzuki, Y. Takeuchi, S. Kawaguchi, M. Kunisu, C. W. Bielawski and Y. Nishina, *Chem. Mater.*, 2017, **29**, 2150–2156.
36 X. Zhu, Y. Zhu, S. Murali, M. D. Stoller and R. S. Ruoff, *ACS Nano*, 2011, **5**, 3333–3338.
37 R. T. Downs, K. L. Bartelmehs, G. V. Gibbs and M. B. Boisen, *American Mineralogist*, 1993, **78**, 1104–1107.
38 D. Yang, A. Velamakanni, G. Bozoklu, S. Park, M. Stoller, R. D. Piner, S. Stankovich, I. Jung, D. A. Field, C. A. Ventrice and R. S. Ruoff, *Carbon*, 2009, **47**, 145–152.
39 S. Pei and H.-M. Cheng, *Carbon*, 2012, **50**, 3210–3228.
40 S. Gadipelli and Z. X. Guo, *Progress in Materials Science*, 2015, **69**, 1–60.
41 B. Diby Ossonon and D. Bélanger, *RSC Advances*, 2017, **7**, 27224–27234.
42 Y. Li, B. Ni, X. Li, X. Wang, D. Zhang, Q. Zhao, J. Li, T. Lu, W. Mai and L. Pan, *Nano-Micro Lett.*, 2019, **11**, 60.
43 S. Ikram, S. Dsoke, A. Sarapulova, M. Müller, U. A. Rana and H. M. Siddiqi, *J. Electrochem. Soc.*, 2020, **167**, 100531.

44 H. Zhang, H. Guo, A. Li, X. Chang, S. Liu, D. Liu, Y. Wang, F. Zhang and H. Yuan, *Journal of Energy Chemistry*, 2019, **31**, 159–166.
45 X. Zhang, J. Zhou, C. Liu, X. Chen and H. Song, *J. Mater. Chem. A*, 2016, **4**, 8837–8843.
46 D. Zhou, L.-P. Xue and N. Wang, *ChemElectroChem*, 2019, **6**, 1552–1557.
47 W. Luo, C. Bommier, Z. Jian, X. Li, R. Carter, S. Vail, Y. Lu, J.-J. Lee and X. Ji, *ACS Appl. Mater. Interfaces*, 2015, **7**, 2626–2631.